Charge–Discharge Performance of Copper Metal Positive Electrodes in Fluorohydrogenate Ionic Liquids for Fluoride-Shuttle Batteries

AUTHOR(S):

Yamamoto, Takayuki; Matsumoto, Kazuhiko; Hagiwara, Rika; Nohira, Toshiyuki

CITATION:

Yamamoto, Takayuki ...[et al]. Charge–Discharge Performance of Copper Metal Positive Electrodes in Fluorohydrogenate Ionic Liquids for Fluoride-Shuttle Batteries. Journal of The Electrochemical Society 2021, 168(4): 040530.

ISSUE DATE:

2021-04

URL:

http://hdl.handle.net/2433/265273

Charge–Discharge Performance of Copper Metal Positive Electrodes in Fluorohydrogenate Ionic Liquids for Fluoride-shuttle Batteries

Takayuki Yamamoto,[1,*,z] Kazuhiko Matsumoto,[2,*] Rika Hagiwara,[2,*] Toshiyuki Nohira[1,*,z]

[1] *Institute of Advanced Energy, Kyoto University, Gokasho, Uji, Kyoto 611-0011, Japan*

[2] *Graduate School of Energy Science, Kyoto University, Sakyo-ku, Kyoto 606-8501, Japan*

*Electrochemical Society Member.

[z]E-mail: yamamoto.takayuki.2w@kyoto-u.ac.jp (T.Y.), nohira.toshiyuki.8r@kyoto-u.ac.jp (T.N.)

Abstract

In search of room-temperature electrolytes for fluoride-shuttle batteries, fluorohydrogenate ionic liquids (FHILs) have emerged, showing high ionic conductivities and better operational practicality. To enhance the performance of these electrolytes, the charge–discharge behavior of copper metal as positive electrodes in FHILs was investigated in this study. In the $[C_2C_1im][(FH)_{2.3}F]$ (C_2C_1im = 1-ethyl-3-methylimidazolium) FHIL electrolyte, although the 1st discharge capacity of 599 mAh $(g\text{-}Cu)^{-1}$ included the reductive reaction of surface oxide films, the 2nd discharge capacity of 444 mAh $(g\text{-}Cu)^{-1}$ that corresponds to 53% of the theoretical capacity was achieved. However, the capacity declines to 167 mAh $(g\text{-}Cu)^{-1}$ at the 20th cycle, indicating low capacity retention. In contrast, the adoption of $[C_2C_1pyrr][(FH)_{2.3}F]$ (C_2C_1pyrr = *N*-ethyl-*N*-methylpyrrolidinium) electrolyte confers improved cycleability across the cycles with a higher discharge capacity of 210 mAh $(g\text{-}Cu)^{-1}$ at the 20th cycle. Scanning electron microscopy and energy-dispersive X-ray spectroscopy performed on the electrode surfaces confirm reduced electrode degradation characterized by suppressed aggregation of copper particles in $[C_2C_1pyrr][(FH)_{2.3}F]$ due to its low CuF_2 solubility compared with $[C_2C_1im][(FH)_{2.3}F]$. Herein, we demonstrate the use of FHILs with low CuF_2 solubilities as a strategy for improving the charge–discharge performance of copper metal positive electrodes in fluoride-shuttle batteries.

Introduction

To break away from the conventional energy supplying system based on fossil fuels, the utilization of renewable energy resources has been spreading all over the world. However, because of the intermittent and unstable power generation of these resources, tremendous amounts of energy storage devices have to be installed to realize next-generation energy supplying system. Although rechargeable batteries are promising candidates for use in combination with renewable energy resources, further development of novel batteries of high energy densities are desirable to meet the increasing demand of large-scaled stationary batteries.

Fluoride-shuttle batteries (FSBs) are getting much attention as one of the next-generation batteries owing to their superior energy densities to current lithium-ion batteries.[1,2] Concerning the development of FSB electrolytes, inorganic solid electrolytes such as $MSnF_4$ (M = Pb, Ba) [3–5] and $La_{1-x}Ba_xF_{3-x}$ ($0 \leq x \leq 1$) [6–11] have been intensively studied for recent several decades. However, in general, these electrolytes require high temperature battery operation at around 423 K, rendering them unsuitable for most practical applications. Thus, several research groups including us have reported electrolytes that enable room-temperature FSB operation.[12–17]

We focused on fluorohydrogenate ionic liquids (FHILs) for FSB electrolytes due to their exceptionally high ionic conductivities in the presence of fluorohydrogenate anions, $[(FH)_nF]^-$.[18,19] For example, $[C_2C_1im][(FH)_{2.3}F]$ (C_2C_1im = 1-ethyl-3methylimidazolium) and $[C_2C_1pyrr][(FH)_{2.3}F]$ (C_2C_1pyrr = *N*-ethyl-*N*-methylpyrrolidinium) exhibit ionic conductivities of 100 and 74.6 mS cm^{-1} at 298 K, respectively.[20,21] Our research group has applied the FHILs to various electrochemical devices including fuel cells[22–24] and capacitors[25–27]. Concerning applications as FSB electrolytes, we recently reported charge–discharge characteristics of CuF_2

positive electrode in $[C_2C_1im][(FH)_{2.3}F]$, in which CuF_2 electrodes exhibited high initial charge and discharge capacities of 517 and 475 mAh $(g\text{-}CuF_2)^{-1}$ corresponding to 98 and 90% of the theoretical capacity (528 mAh $(g\text{-}CuF_2)^{-1}$), respectively.[28] However, in general, toward practical application of rechargeable batteries, positive electrodes should be initiated from the discharged state, *i.e.*, copper metal, due to high reactivity of charged compounds with moisture. According to the previous study[14], copper metal exhibited reversible capacities of less than 80 mAh g^{-1} in ether-based electrolytes at room temperature, which is approximately as low as 10% of the theoretical capacity (844 mAh $(g\text{-}Cu)^{-1}$). Since our previous study revealed that FHILs give higher utilization ratios of CuF_2 positive electrodes for FSBs, the improved performance is also expected for copper metal positive electrodes in FHIL electrolytes. Thus, in this study, we examined the charge–discharge tests of copper metal electrodes at room temperature in two FHILs: $[C_2C_1im][(FH)_{2.3}F]$ and $[C_2C_1pyrr][(FH)_{2.3}F]$.

Experimental

The fluorohydrogenate ionic liquids, $[C_2C_1im][(FH)_{2.3}F]$ and $[C_2C_1pyrr][(FH)_{2.3}F]$, and their precursors, $[C_2C_1im]Cl$ and $[C_2C_1pyrr]Cl$, were purchased from Morita Chemical Industries Co., Ltd. and Yoyulabo Co., Ltd., respectively. A three-electrode cell (EC Frontier Co., Ltd.) was used for the electrochemical measurements. Copper composite films on platinum mesh current collectors were used as the working electrodes. The copper composite films are composed of copper metal powder (Aldrich, 60–80 nm), acetylene black (AB; Strem Chemicals), and polytetrafluoroethylene (PTFE; Aldrich) at a weight ratio of 60:20:20. After mixing and grinding these powders in a mortar, the resultant composite film was pressed on a

platinum mesh. Mixed electrodes made from CuF_2 (Alfa Acer, purity 99.5%), copper metal, AB, and PTFE with a weight ratio of 50/35/10/5 (or 40/30/15/15) were used as the reference and counter electrodes. A two-ply PTFE filter (Omnipore^{TM}, Millipore, thickness: 65 μm, average pore diameter: 0.45 μm, porosity: 80%) was used as a separator. All electrodes and PTFE filters were immersed in the electrolyte prior to the test.

Cyclic voltammetry and charge–discharge tests were conducted using electrochemical measurement apparatus (HZ-7000 or HZ-Pro, Hokuto Denko Corp.) at 298 K. Charge–discharge tests were started after cyclic voltammetry test for three cycles at a scan rate of 10 mV s^{-1}. Charge–discharge rate was fixed at 0.05C (= 42.2 mA $(g\text{-}Cu)^{-1}$). Potentials are described as those with respect to the redox couple of CuF_2/Cu. Further details on the conditions are provided in the text or figure captions.

To identify the existing phases of the copper metal electrodes before and after charge–discharge tests, X-ray diffraction (XRD) analysis was performed using an X-ray diffractometer (Ultima IV, Rigaku Co.; Cu-$K\alpha$ radiation (λ = 1.5418 Å)) equipped with a 1D high-speed detector (D/teX Ultra, Rigaku Co.) and a nickel filter. An X-ray photoelectron spectrometer (XPS; JPS-9010, JEOL) combined with argon ion etching was used to analyze the elemental compositions and chemical states of the electrodes. The accelerating voltage, current, and argon ion etching time were 0.017 kV, 0.3 mA, and 10 s, respectively. The surface morphologies and existing elements were investigated by a field emission scanning electron microscope (FE-SEM; SU-6600, Hitachi) equipped with an energy-dispersive X-ray spectroscope (EDX; EMAX x-act, Horiba).

Before the analysis, the electrochemical cells were disassembled and the remaining

electrolytes on the surfaces of copper metal electrodes were removed by soaking the samples in dehydrated and deoxidized ethanol (water content < 10 ppm, oxygen content < 1 ppm; Wako Pure Chemical Industries, Ltd.). Here, handling was done in an argon-filled glovebox. Finally, the samples were transferred to the XRD, XPS and FE-SEM analysis or work chambers without air exposure.

The solubility of CuF_2 in ionic liquid electrolytes was determined by inductively coupled plasma atomic emission spectroscopy (ICP-AES; SPECTRO BLUE, Hitachi) as follows: First, CuF_2 powder was added into $[C_2C_1im][(FH)_{2.3}F]$ and $[C_2C_1pyrr][(FH)_{2.3}F]$ ionic liquids and stirred at 298 K for 24 h. Then, the remaining powder was removed by filteration and the liquid was diluted by adding 0.1 mol dm^{-3} nitric acid aqueous solution. Finally, the concentration of copper in the solution was measured by ICP-AES.

Results and Discussion

The redox behavior of a copper metal electrode in $[C_2C_1im][(FH)_{2.3}F]$ FHIL electrolytes was investigated by cyclic voltammetry at 298 K, as shown in Fig. 1a. In the 1st cycle, oxidative currents were observed to gradually increase from the rest potential (~0 V vs. CuF_2/Cu), with a large hump appearing in the 0–0.7 V potential region. Then, the scan to the negative potential revealed a sharp reduction peak below 0 V. For the 2nd cycle, an oxidation current peak emerged at around 0.1 V accompanied by a current shoulder above 0.4 V while no significant changes were detected in the reduction behavior during the negative potential scan. As affirmed by our previous study on CuF_2 positive electrodes in the $[C_2C_1im][(FH)_{2.3}F]$ electrolyte, [28] the oxidation and reduction currents observed can be ascribed to the fluorination and defluorination

of copper metal, respectively, in accordance with the following reaction:

$$Cu + 6[(FH)_2F]^- \rightleftharpoons CuF_2 + 4[(FH)_3F]^- + 2e^- \quad (1)$$

As shown in Fig. 1b, the 1st cycle reached a charge (oxidative) capacity of 439 mAh $(g\text{-}Cu)^{-1}$, which corresponds to 52% of the theoretical capacity (844 mAh $(g\text{-}Cu)^{-1}$), along with a discharge (reductive) capacity of 599 mAh $(g\text{-}Cu)^{-1}$. The significantly higher discharge capacity than the charge capacity observed here can be attributed to an irreversible reductive reaction of oxide films on the surface of copper particles. Accordingly, this test confirms that the charge–discharge performance of a copper metal electrode in $[C_2C_1im][(FH)_{2.3}F]$ IL electrolyte at room temperature is superior to the previously reported ether-based electrolytes, which only achieved 10% of the theoretical capacity (see Introduction section).[14] It further affirms the positive influence of the $[(FH)_nF]^-$ anions on the charge–discharge performance of the $[C_2C_1im][(FH)_{2.3}F]$ IL electrolyte.

To confirm the structural changes occurring in the positive electrodes during the initial cycle, XRD analysis was performed on the copper metal electrodes along with the platinum current collectors at different charge states (*i.e.*, (a) pristine state, (b) after charging to 0.7 V vs. CuF_2/Cu and (c) after 1 cycle at −0.3 V vs. CuF_2/Cu) as shown in Fig. 2. In the pristine state (Fig. 2a), diffraction peaks of copper metal and platinum current collector were detected as should be expected. Upon charging (Fig. 2b), the peak intensities of copper significantly decrease with respect to platinum current collector, suggesting the occurrence of the fluorination reaction of the copper metal. However, no peaks assignable to copper difluoride are observed, indicative of the amorphous nature of the copper difluoride formed. Such phenomena were already proved by our previous report on CuF_2 positive electrodes in this

$[C_2C_1im][(FH)_{2.3}F]$ IL electrolyte[28]. The remaining copper peaks suggest the presence of unreacted active material since the 1st charge capacity does not reach the theoretical value. Upon completing the cycle, the copper peaks are seen to recover, as shown in Fig. 2c, which indicates the reversibility of the reaction involving the active material.

For further discussion of the chemical changes occurring in the positive electrodes during the initial cycle, X-ray photoelectron spectra of the copper metal electrodes in the Cu 2p region were obtained at the different charge–discharge states mentioned above, as shown in Fig. 3. In the pristine electrode (Fig. 3a), copper metal peaks appear at binding energies of ~932 eV and ~952 eV, with peak shoulders assignable to CuO. This indicates the formation of an oxide film on the surface of the copper particles, which corresponds to the larger discharge capacities observed in the 1st cycle (Fig. 1b). Upon charging (Fig. 3b), new peaks corresponding to Cu $2p_{3/2}$ and Cu $2p_{1/2}$ in CuF_2 emerge at the binding energies of ~937 eV and ~957 eV, respectively.[29] Likewise, a peak shoulder remains at around 932 eV, assignable to unreacted active material. After the first cycle (Fig. 3c), the CuF_2 peaks almost disappeared while the copper metal peaks are recovered back at their original peak positions. The peak shoulders corresponding to CuO are not detected after discharge, which is consistent with the irreversible capacity of the 1st cycle.

In order to elucidate the detailed charge–discharge mechanisms of the copper metal positive electrodes in $[C_2C_1im][(FH)_{2.3}F]$ electrolyte at 298 K, further cycling was conducted for 20 cycles. As can be seen in Fig. 4a, the charge profile of the 2nd cycle exhibits a higher charge capacity of 528 mAh $(g\text{-}Cu)^{-1}$ with lower polarization than that in the 1st cycle, indicating the disappearance of the oxide film on the surface of the active material. The detailed

cycling properties of the copper metal positive electrode are provided in Fig. 4b. The discharge capacity is observed to rapidly decrease from 444 mAh $(g\text{-}Cu)^{-1}$ at the 2nd cycle to 259 mAh $(g\text{-}Cu)^{-1}$ at the 5th cycle, suggesting the occurrence of significant electrode degradation as a result of the conversion reaction from copper metal to CuF_2. Then, the discharge capacity has gradually decreased to 167 mAh $(g\text{-}Cu)^{-1}$ at the 20th cycle.

In order to understand the degradation mechanisms of the copper metal positive electrodes, a closer look into the dissolution reactions occurring during battery operations would be insightful. According to our previous study[28], a small amount of CuF_2 chemically dissolves into $[C_2C_1im][(FH)_{2.3}F]$ electrolyte up to ca. 100 ppm (= (mg-Cu) dm^{-3}) and re-precipitation of the dissolved CuF_2 on the electrode surface occurs simultaneously, which realizes smooth defluorination/fluorination reactions.

During the charge process of copper metal electrode, copper difluoride formed by the direct fluorination expressed as the Eq. (1) is likely to dissolve into the FHIL electrolyte as follows:

$$CuF_2 + 2[(FH)_2F]^- \rightleftharpoons [CuF_4]^{2-} + 4HF \qquad (2)$$

The produced HF can immediately react with $[(FH)_2F]^-$ to form $[(FH)_3F]^-$. Besides the direct fluorination reaction of copper metal, the electrochemical dissolution of copper metal could also occur on the electrode surface.

$$Cu + 12[(FH)_2F]^- \rightleftharpoons [CuF_4]^{2-} + 8[(FH)_3F]^- + 2e^- \qquad (3)$$

Although the dissolved species of CuF_2 in this electrolyte cannot be detected due to extremely low CuF_2 solubility, we speculate the existence of $[CuF_4]^{2-}$ ion from previous reports on several compounds such as K_2CuF_4[30] and Cs_2CuF_4[31]. Besides, we should note that the $[CuF_4]^{2-}$ unit in

these compounds is not a discrete ion, in which one copper atom is octahedrally coordinated by six fluorine atoms, sharing four fluorine atoms with an adjacent $[CuF_4]^{2-}$ unit. Concerning the Eqs. (2) and (3), we assume that the discrete $[CuF_4]^{2-}$ ion exists in this highly fluorobasic ionic liquid. There could be other candidates of complex ions, in which other ligands additionally coordinate copper atoms to form octahedral complexes. These are still under investigation. According to Eq. (2), $[CuF_4]^{2-}$ ion exists in equilibrium with CuF_2. When the concentration of $[CuF_4]^{2-}$ ion at the vicinity of the electrode surface exceeds the solubility of copper in the electrolyte, the produced $[CuF_4]^{2-}$ instantly precipitates as CuF_2 on the electrode surface.

During discharge process, reverse reactions of Eqs. (1) and (3) simultaneously proceed and copper metal is recovered on the electrode surface. However, such a dissolution/precipitation mechanism also tends to induce morphological changes that could influence the behavior of the active material. This is because CuF_2 formed in the charge process is likely to be unevenly distributed across the electrode surface and resultant copper metal distribution after discharge process reflects the surface conditions of the charged state.

In this way, the solubility of CuF_2 in electrolytes is considered to affect the cycling performance of the copper metal positive electrode. In fact, a similar strategy has been proposed for ether-based electrolytes in fluoride-shuttle batteries,[13,15] where the cycling performance of bismuth fluoride (BiF_3) positive electrodes was found to improve in electrolytes with a low solubility of BiF_3[15]. Thus, we adopted a new FHIL electrolyte, $[C_2C_1pyrr][(FH)_{2.3}F]$, with a lower solubility of CuF_2. ICP-AES analysis revealed the solubility of CuF_2 in $[C_2C_1pyrr][(FH)_{2.3}F]$ to be significantly lower (ca. 20 ppm) compared to

$[C_2C_1im][(FH)_{2.3}F]$, which was previously reported to be ca. 100 ppm[28]. Therefore, an improvement in the charge–discharge behavior of the copper metal positive electrode can be expected using the $[C_2C_1pyrr][(FH)_{2.3}F]$ electrolyte.

To investigate the performance of copper metal positive electrodes in $[C_2C_1pyrr][(FH)_{2.3}F]$ at 298 K, charge–discharge profiles were obtained in the course of 20 cycles, as shown in Fig. 5a. The 1st charge capacity of 319 mAh $(g\text{-}Cu)^{-1}$ is lower than that in the case of $[C_2C_1im][(FH)_{2.3}F]$ electrolyte, which can be ascribed to the lower CuF_2 solubility in $[C_2C_1pyrr][(FH)_{2.3}F]$ electrolyte. Furthermore, a large polarization is observed at the beginning of the initial charge profile, which is not in the case of $[C_2C_1im][(FH)_{2.3}F]$ IL. Since the CuF_2 solubility into $[C_2C_1pyrr][(FH)_{2.3}F]$ IL is much lower than that into $[C_2C_1im][(FH)_{2.3}F]$ IL, the polarization affirms the sluggish kinetics of the CuF_2 dissolution/re-precipitation reactions in the $[C_2C_1pyrr][(FH)_{2.3}F]$ electrolyte, compared with that in the $[C_2C_1im][(FH)_{2.3}F]$ electrolyte. Despite the differences in solubility, the 1st cycle reaches a significantly higher discharge capacity of 400 mAh $(g\text{-}Cu)^{-1}$, implicit of a reaction mechanism similar to the aforementioned $[C_2C_1im][(FH)_{2.3}F]$ electrolyte (*i.e.*, the irreversible reduction reaction of the oxide films on the surface of the active material). As shown in the cycling characteristics curves in Fig. 5b, the 2nd cycle in the $[C_2C_1pyrr][(FH)_{2.3}F]$ electrolyte gives a lower discharge capacity of 361 mAh $(g\text{-}Cu)^{-1}$ than in the case of the $[C_2C_1im][(FH)_{2.3}F]$ electrolyte. In addition, when compared between Figs. 4a and 5a, the polarization of charging plateaus after 2nd cycle is slightly larger than that in $[C_2C_1im][(FH)_{2.3}F]$ electrolyte, which indicates the slower fluorination kinetics of copper in $[C_2C_1pyrr][(FH)_{2.3}F]$ electrolyte. However, the cycling properties of the copper metal electrode in the newly adopted $[C_2C_1pyrr][(FH)_{2.3}F]$ electrolyte are superior to those in the

previous electrolyte $[C_2C_1im][(FH)_{2.3}F]$. The discharge capacities at 20th cycle are 167 and 210 mAh $(g\text{-}Cu)^{-1}$ in $[C_2C_1im][(FH)_{2.3}F]$ and $[C_2C_1pyrr][(FH)_{2.3}F]$ electrolytes, respectively. Thus, $[C_2C_1pyrr][(FH)_{2.3}F]$ achieves a higher capacity retention of 58% at the 20th cycle with respect to the 2nd cycle, compared with the case of the $[C_2C_1im][(FH)_{2.3}F]$ electrolyte (38% at the 20th cycle). The improved performance in $[C_2C_1pyrr][(FH)_{2.3}F]$ is also reflected to the Coulombic efficiencies during 20 cycles. The average Coulombic efficiencies of copper metal electrodes between 2nd and 20th cycles are 91 and 95% for $[C_2C_1im][(FH)_{2.3}F]$ and $[C_2C_1pyrr][(FH)_{2.3}F]$ electrolytes, respectively. The higher average cycling efficiency in the $[C_2C_1pyrr][(FH)_{2.3}F]$ electrolyte supports the superior capacity retention for 20 cycles.

To further elucidate the underlying mechanisms behind the different cycling properties, SEM–EDX analyses of the copper metal electrodes cycled in the two FHIL electrolytes for 20 cycles, the fully discharged state, were conducted, as shown in Fig. 6. In the pristine electrode (Fig. 6a), copper particles appear to be homogeneously distributed on the electrode surface. However, after 20 cycles in the respective electrolytes, distinct differences are observed on the copper electrode surfaces. As illustrated by the EDX mapping of the copper electrode in the $[C_2C_1im][(FH)_{2.3}F]$ electrolyte (Fig. 6b), large copper particles, several micrometers in size, are found to be unevenly distributed on the electrode surface. This distribution indicates to the continued aggregation of copper during the fluorination and defluorination cycles. Since the solubility of CuF_2 in the $[C_2C_1im][(FH)_{2.3}F]$ electrolyte is higher, the electrochemical dissolution of copper metal and chemical dissolution of CuF_2 are likely to occur simultaneously in the charge process, resulting in the dissipation of active materials from their original position on the surface. The dissolved copper species easily diffuse in the electrolyte and migrate from

their original position to preferentially precipitate on CuF_2 active materials. Then, in the discharge process, the copper metal is unevenly produced across the electrode surface, resulting in the progressive aggregation of copper with continued cycling.

There might be one remaining concern for the uneven distribution of copper on the electrode surface; disappearance of copper could be ascribed to the dissolution of copper into the bulk electrolyte. However, the solubility of CuF_2 is as low as 100 (mg-Cu) dm^{-3} and the volume of the electrolyte is approximately 4×10^{-4} dm^3 per cell, from which the maximum amount of dissolved copper is calculated to be 4×10^{-2} mg, according to the following equation:

$$W_{Cu(sol)} = C_{Cu(ICP\text{-}AES)} \times V_{Electrolyte} \quad (4)$$

where $W_{Cu(sol)}$ is the mass of copper dissolved in the electrolyte (mg-Cu), $C_{Cu(ICP\text{-}AES)}$ is the concentration of copper determined by the ICP-AES analysis ((mg-Cu) dm^{-3}), and $V_{Electrolyte}$ is the volume of electrolyte in the electrochemical cell (dm^3), respectively. Since the used copper metal in the working electrode is ca. 1.5 mg per cell, no more than 2.7 wt% of copper metal in the working electrode can be dissolved into the electrolyte. Consequently, dissolution of copper into the electrolyte cannot validate the disappearance of copper in more than half area of the electrode surface.

On the other hand, the EDX mapping of the copper metal electrode after cycling in the $[C_2C_1pyrr][(FH)_{2.3}F]$ electrolyte (Fig. 6c) exhibits improved homogeneity in the distribution of copper particles across the entire electrode surface, which proves suppressed aggregation of copper during the cycling. Owing to the low solubility of CuF_2 in $[C_2C_1pyrr][(FH)_{2.3}F]$, diffusion of the copper species formed by electrochemical dissolution of copper metal and chemical dissolution of CuF_2 would also be limited, implying that re-precipitation also occurs

in the vicinity of the original position. Consequently, the uniformity of the resultant electrode surface is enhanced, which is a plausible explanation for the improved capacity retention of the copper metal electrode in the $[C_2C_1pyrr][(FH)_{2.3}F]$ electrolyte. Based on the charge–discharge properties observed in Fig. 5b, the solubility of CuF_2 in FHIL electrolytes is deduced to have a large impact not only on the initial reversible capacities but also on the cycleability of the copper metal electrode. Finally, it should be noted that the amount of the dissolved copper species is very small in $[C_2C_1pyrr][(FH)_{2.3}F]$ IL. Since the solubility of CuF_2 in $[C_2C_1pyrr][(FH)_{2.3}F]$ is ca. 20 ppm from ICP-AES results, only 0.53 wt% of copper metal in the working electrode can be dissolved into this IL, based on the similar calculation using the Eq. (4). Considering the results of SEM–EDX analyses, this small amount of dissolution of copper induces no fatal changes on the surface of the copper metal electrode.

As the initial reversible capacities and the cycleability of the positive electrode prove to be crucial parameters for the evaluation of battery performance, their trade-off relationship with regards to the solubility of CuF_2 presents a key platform for the exploration of optimized FSB electrolytes used with copper metal electrodes.

Conclusions

In this study, we investigated the electrochemical performance of copper metal as positive electrodes for FSBs in two different FHIL electrolytes. In $[C_2C_1im][(FH)_{2.3}F]$, higher capacities were obtained in the 1st and 2nd cycles, however, the significant capacity decline occurred afterwards. Although copper metal electrode in $[C_2C_1pyrr][(FH)_{2.3}F]$ achieves lower initial capacities, its cycleability and capacity retention are improved. These differences in charge–

discharge performance are ascribed to the differences in the solubility of CuF_2 in the two FHILs. The low solubility of CuF_2 in $[C_2C_1pyrr][(FH)_{2.3}F]$ effectively suppresses the aggregation of the active materials as confirmed by the homogenous distribution of copper particles observed in the SEM–EDX results of the electrode surfaces. This work provides a vital platform for future studies on the optimization of positive electrode performance in FSBs.

Acknowledgments

This study is based on results obtained from a project, "Research and Development Initiative for Scientific Innovation of New Generation Batteries (RISING2)", JPNP16001, commissioned by the New Energy and Industrial Technology Development Organization (NEDO), Japan.

References

1. F. Gschwind, G. Rodriguez-Garcia, D. J. S. Sandbeck, A. Gross, M. Weil, M. Fichtner, N. Hörmann, *J. Fluorine Chem.*, **182**, 76 (2016).
2. G. Karkera, M. A. Reddy, M. Fichtner, *J. Power Sources*, **481**, 228877 (2021).
3. I. Mohammad, R. Witter, M. Fichtner, M. A. Reddy, *ACS Appl. Energy Mater.*, **1**, 4766 (2018).
4. L. Liu, L. Yang, M. Liu, X.Li, D. Shao, K. Luo, X. Wang, Z. Luo, *J. Alloys Comp.*, **819**, 152983 (2020).
5. Y. Matsuo, J. Inamoto, A. Mineshige, M. Murakami, K. Matsumoto, R. Hagiwara, *Electrochem. Commun.*, **110**, 106626 (2020).
6. J. Schoonman, A. Wolfert, *Solid State Ionics*, **3–4**, 373 (1981).
7. M. A. Reddy and M. Fichtner, *J. Mater. Chem.*, **21**, 17059 (2011).
8. N. M. Ali, W. Kerstin, R. Jochen, M. A. Reddy, C. Oliver, *Chem. Mater.*, **29**, 3441 (2017).

9. D. T. Thieu, M. H. Fawey, H. Bhatia, T. Diemant, V. S. K. Chakravadhanula, R. J. Behm, C. Kübel, M. Fichtner, *Adv. Funct. Mater.*, **27**, 1701051 (2017).
10. A. Grenier, A. G. Porras-Gutierrez, M. Body, C. Legein, F. Chrétien, E. Raymundo-Piñero, M. Dollé, H. Groult, D. Dambournet, *J. Phys. Chem. C*, **121**, 24962 (2017).
11. I. Mohammad, R. Witter, M. Fichtner, M. A. Reddy, *ACS Appl. Energy Mater.*, **2**, 1553 (2019).
12. K. Okazaki, Y. Uchimoto, T. Abe, Z. Ogumi, *ACS Energy Lett.*, **2**, 1460 (2017).
13. H. Konishi, T. Minato, T. Abe, Z. Ogumi, *J. Electrochem. Soc.*, **164**, A3702 (2017).
14. V. K. Davis, C. M. Bates, K. Omichi, B. M. Savoie, N. Momčilović, Q. Xu, W. J. Wolf, M. A. Webb, K. J. Billings, N. H. Chou, S. Alayoglu, R. K. McKenney, I. M. Darolles, N. G. Nair, A. Hightower, D. Rosenberg, M. Ahmed, C. J. Brooks, T. F. Miller III, R. H. Grubbs, S. C. Jones, *Science*, **362**, 1144 (2018).
15. H. Konishi, T. Minato, T. Abe, Z. Ogumi, *J. Appl. Electrochem.*, **48**, 1205 (2018).
16. T. Yamanaka, K. Okazaki, T. Abe, K. Nishio, Z. Ogumi, *ChemSusChem*, **12**, 527 (2019).
17. H. Konishi, T. Minato, T. Abe, Z. Ogumi, *J. Phys. Chem. C*, **123**, 10246 (2019).
18. R. Hagiwara, T. Hirashige, T. Tsuda, Y. Ito, *J. Fluorine Chem.*, **99**, 1 (1999).
19. T. Enomoto, Y. Nakamori, K. Matsumoto, R. Hagiwara, *J. Phys. Chem. C*, **115**, 4324 (2011).
20. R. Hagiwara, T. Hirashige, T. Tsuda, Y. Ito, *J. Electrochem. Soc.*, **149**, D1 (2002).
21. K. Matsumoto, R. Hagiwara, Y. Ito, *Electrochem. Solid-State Lett.*, **7**, E41 (2004).
22. R. Hagiwara, T. Nohira, K. Matsumoto, Y. Tamba, *Electrochem. Solid-State Lett.*, **8**, A231 (2005).
23. J. S. Lee, T. Nohira, R. Hagiwara, *J. Power Sources*, **171**, 535 (2007).
24. P. Kiatkittikul, J. Yamaguchi, R. Taniki, K. Matsumoto, T. Nohira, R. Hagiwara, *J. Power Sources*, **266**, 193 (2014).
25. M. Ue, M. Takeda, A. Toriumi, A. Kominato, R. Hagiwara, Y. Ito, *J. Electrochem. Soc.*, **150**, A499 (2003).
26. A. Senda, K. Matsumoto, T. Nohira, R. Hagiwara, *J. Power Sources*, **195**, 4414 (2010).
27. R. Taniki, K. Matsumoto, T. Nohira, R. Hagiwara, *J. Electrochem. Soc.*, **160**, A734 (2013).
28. T. Yamamoto, K. Matsumoto, R. Hagiwara, T. Nohira, *ACS Appl. Energy Mater.*, **2**, 6153

(2019).

29. G. van der Laan, C. Westra, C. Haas, G. A. Sawatzky, *Phys. Rev. B*, **23**, 4369 (1981).
30. M. J. Riley, L. Dubicki, G. Moran, E. R. Krausz, I. Yamada, *Inorg. Chem.*, **29**, 1614 (1990).
31. J.-M. Dance, J. Grannec, A. Tressaud, *C. R. Acad. Sci.*, **283**, 115 (1976).

Figures

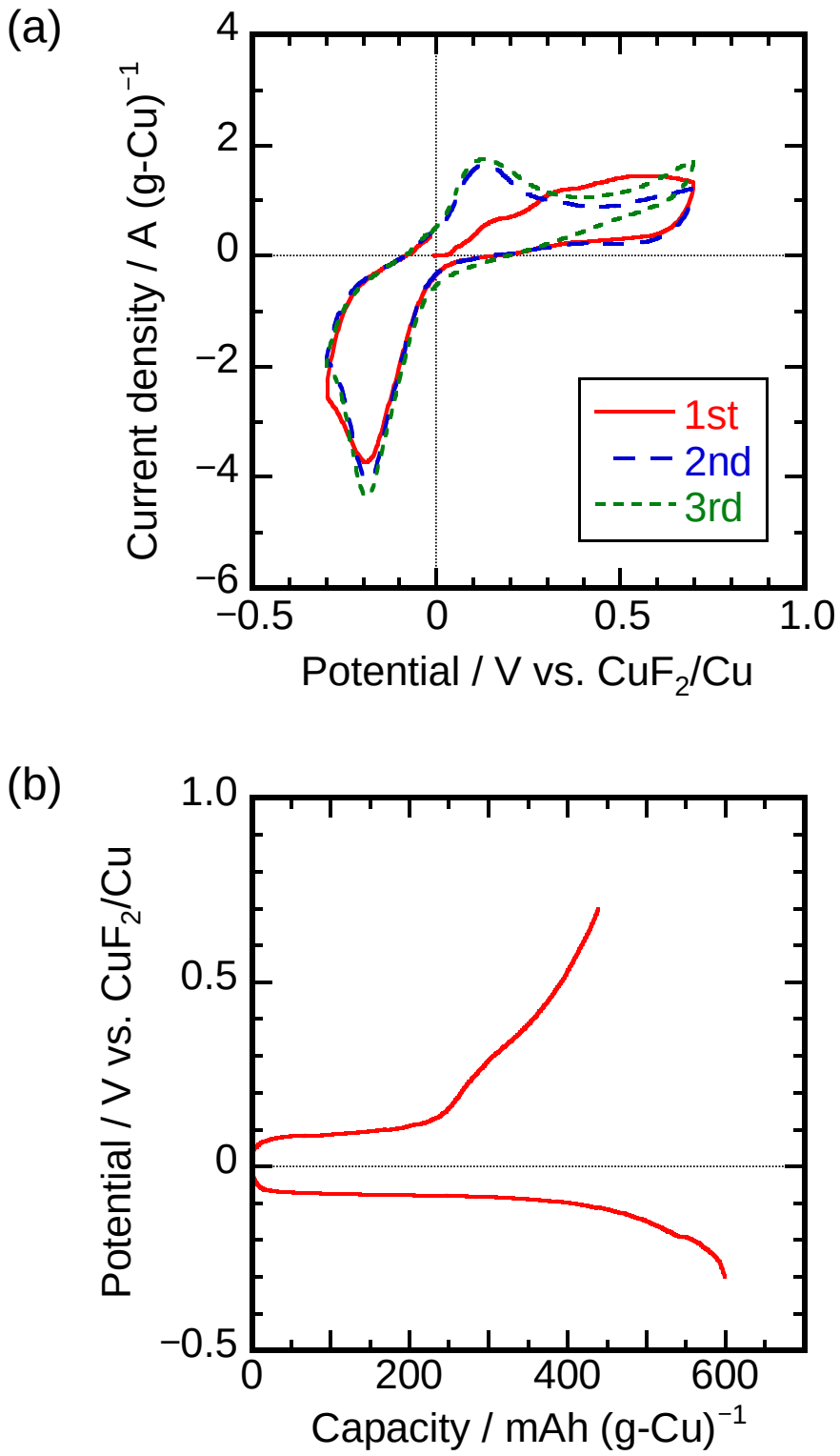

Fig. 1 (a) Cyclic voltammograms and (b) initial charge–discharge curves of the copper metal electrode in the $[C_2C_1im][(FH)_{2.3}F]$ electrolyte at 298 K. Scan rate in (a): 10 mV s^{-1}. Charge–discharge rate in (b): 0.05C.

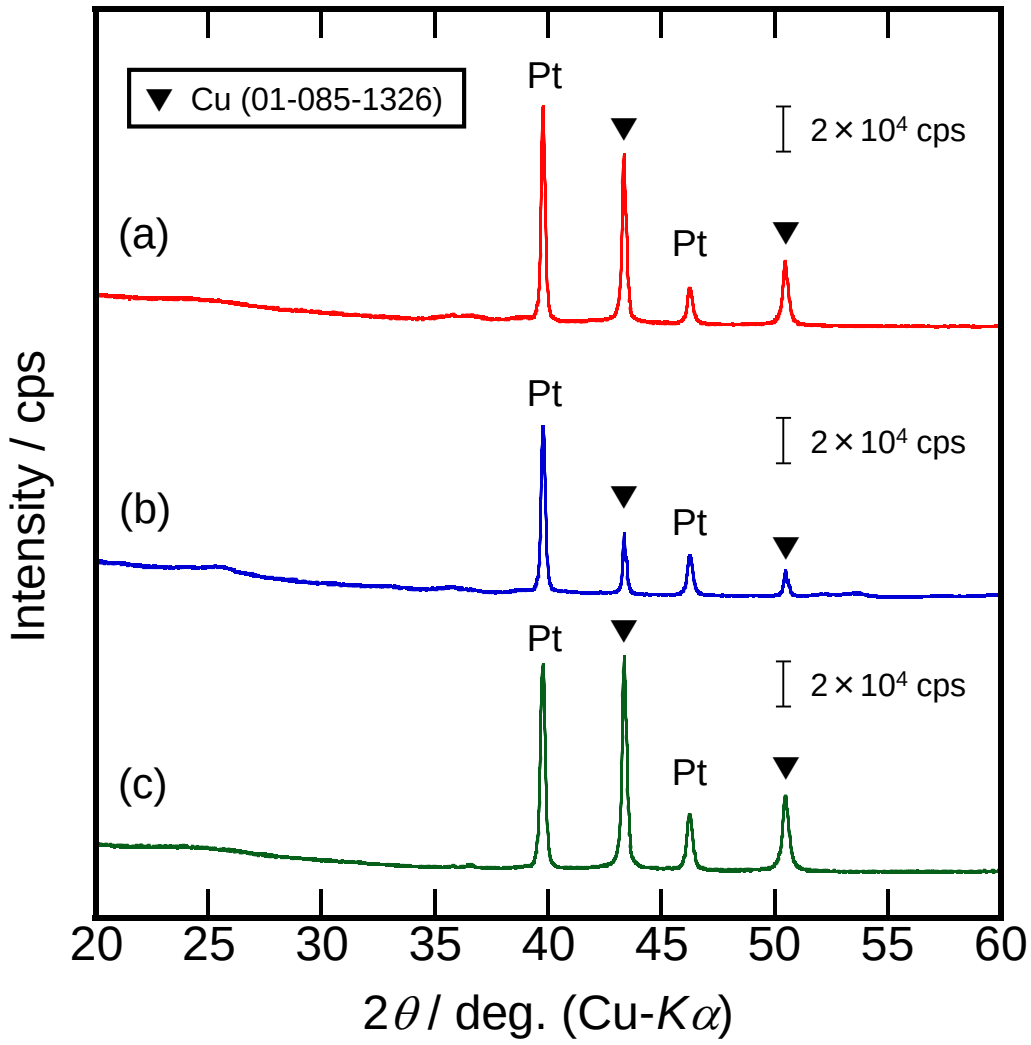

Fig. 2 X-ray diffraction patterns of the copper metal electrodes (a) before charging (pristine state), (b) after charging to 0.7 V vs. CuF_2/Cu, and (c) after 1 cycle to −0.3 V vs. CuF_2/Cu in the $[C_2C_1im][(FH)_{2.3}F]$ electrolyte at 298 K. The diffraction peaks of Pt metal arise from the Pt current collector.

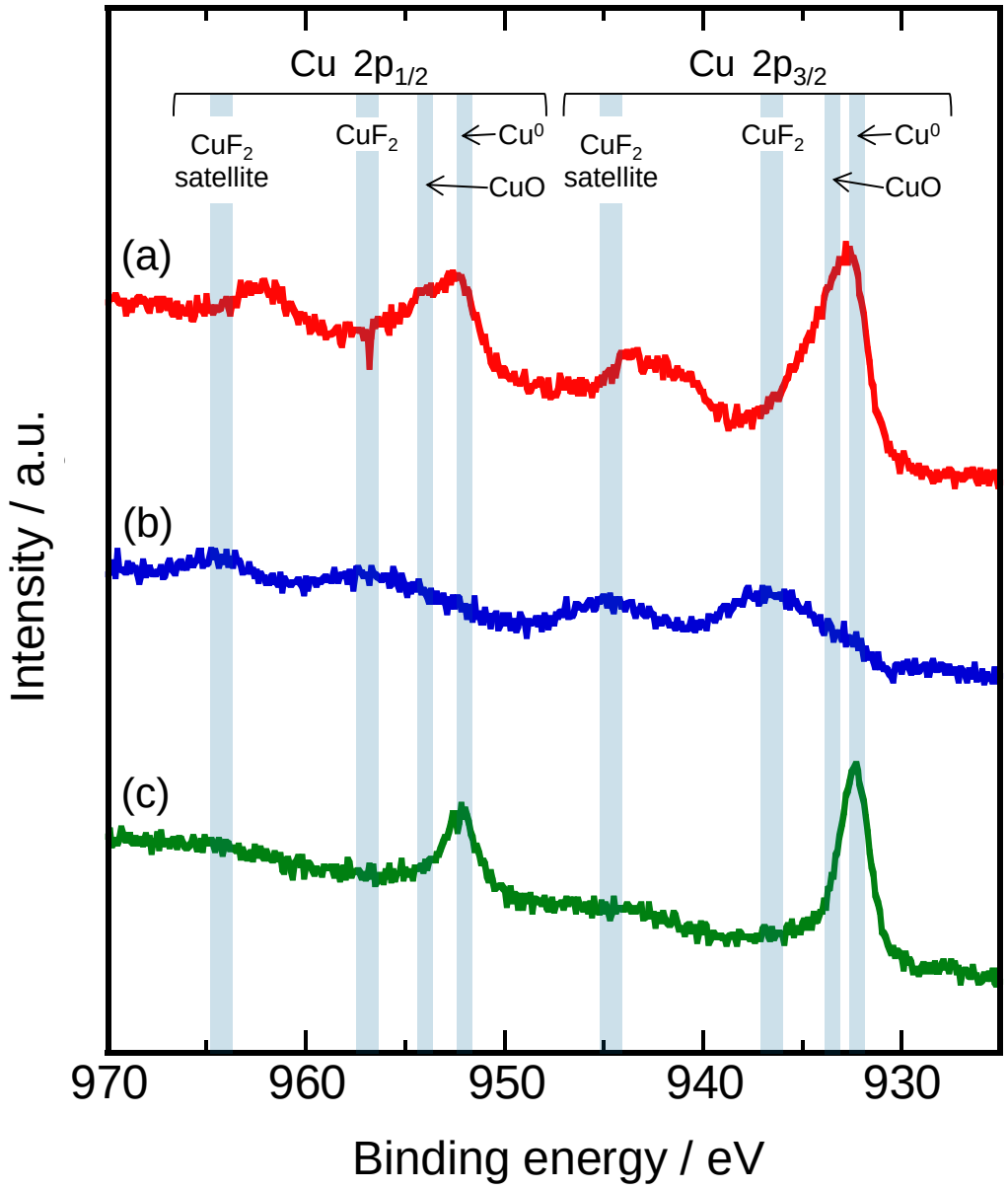

Fig. 3 Cu 2p XPS profiles of the copper metal electrodes (a) before charging (pristine state), (b) after charging to 0.7 V vs. CuF_2/Cu, and (c) after 1 cycle to −0.3 V vs. CuF_2/Cu. in the $[C_2C_1im][(FH)_{2.3}F]$ electrolyte at 298 K.

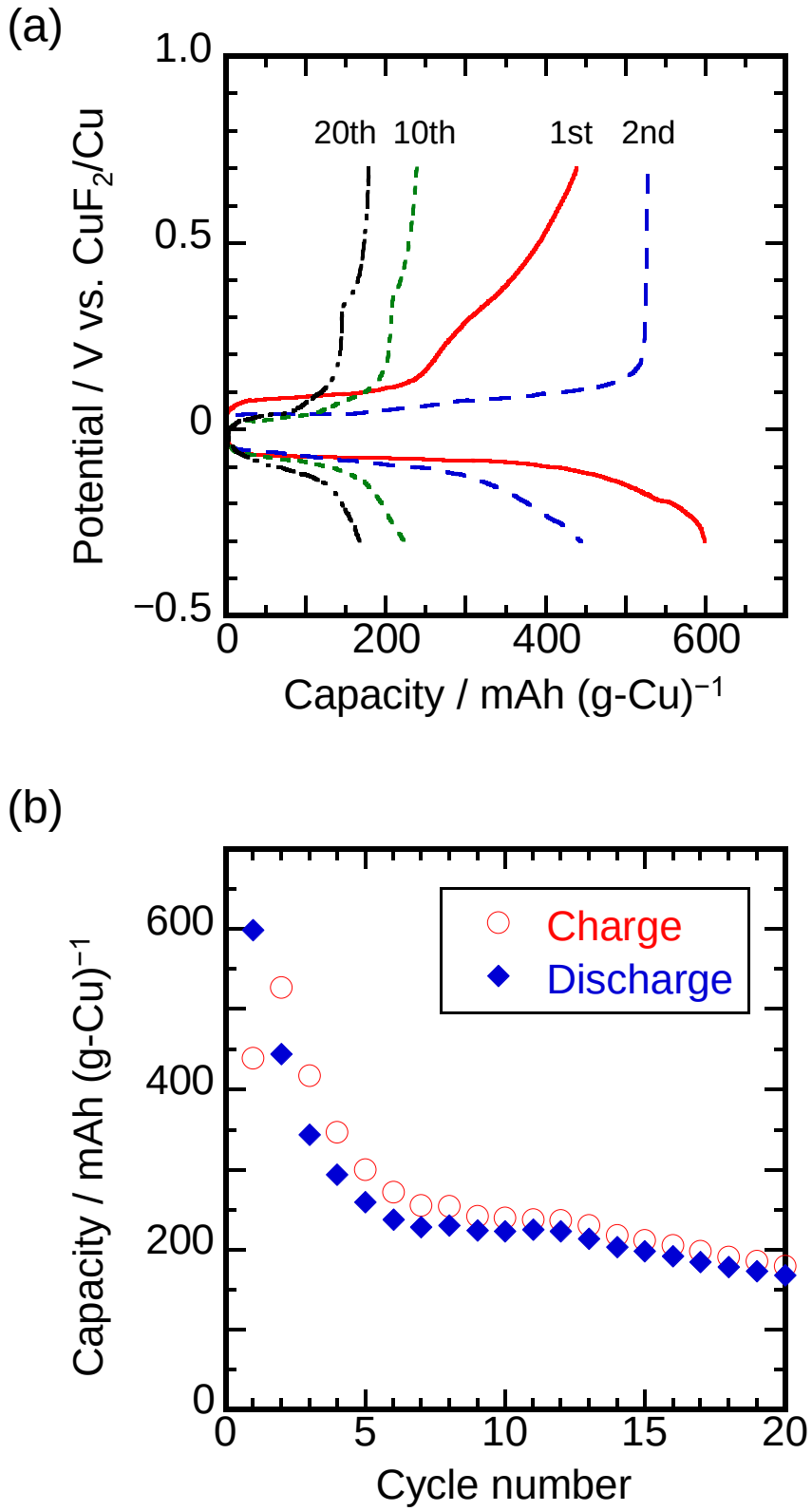

Fig. 4 (a) Charge–discharge curves and (b) cycling characteristics of the copper metal electrode in the $[C_2C_1im][(FH)_{2.3}F]$ electrolyte at 298 K. Charge–discharge rate: 0.05C.

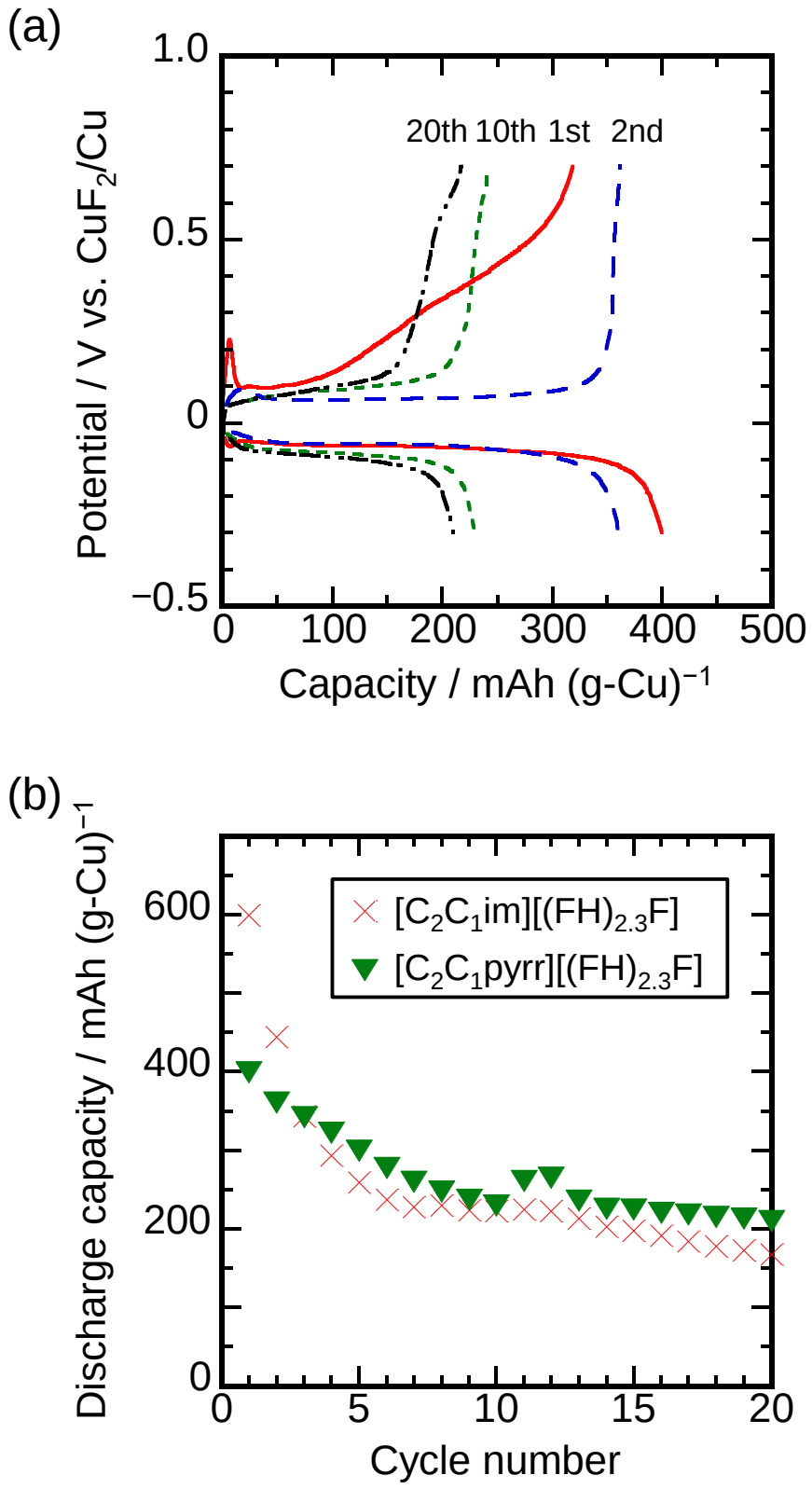

Fig. 5 (a) Charge–discharge curves of the copper metal electrode in $[C_2C_1pyrr][(FH)_{2.3}F]$ electrolyte at 298 K. (b) A comparison of discharge capacities of the copper metal electrode in the $[C_2C_1im][(FH)_{2.3}F]$ and $[C_2C_1pyrr][(FH)_{2.3}F]$ electrolytes at 298 K. Charge–discharge rate: 0.05C.

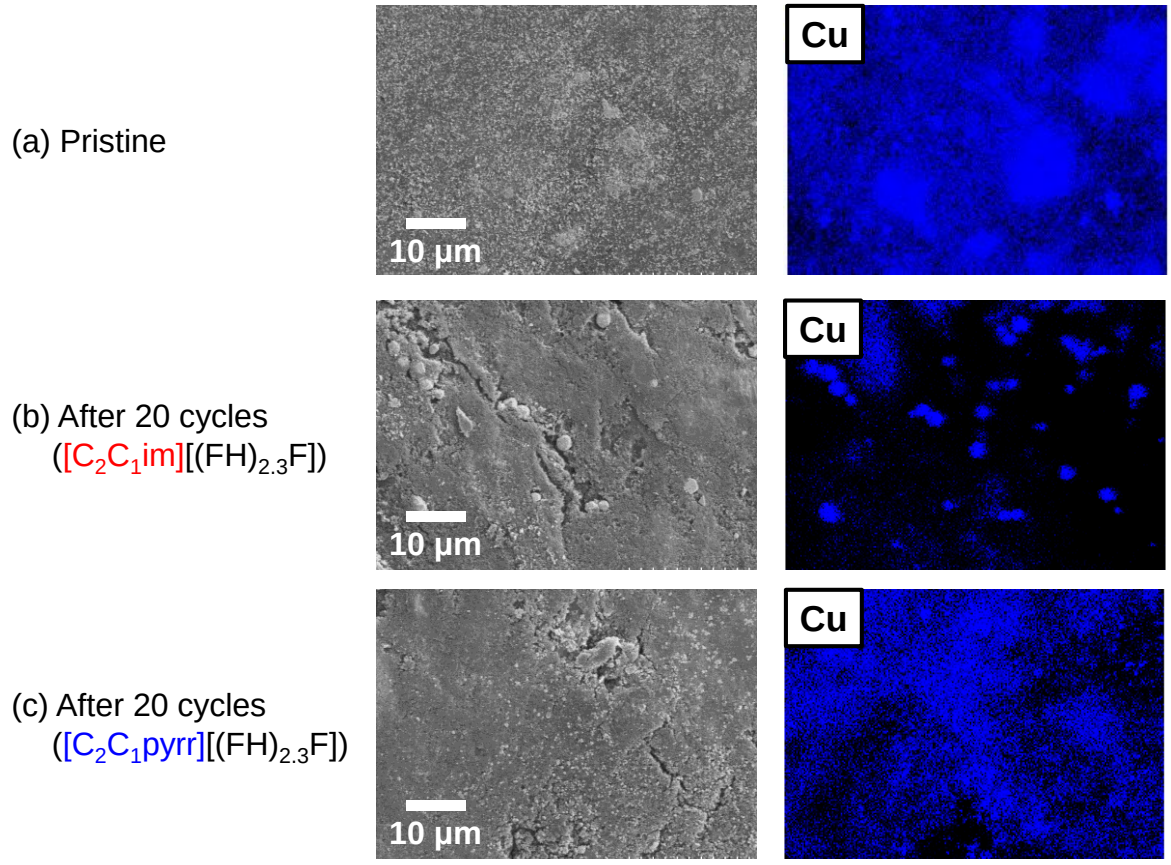

Fig. 6 SEM images and corresponding EDX mapping of the copper metal electrodes surfaces (a) before charging (pristine state), (b) after 20 cycles in the $[C_2C_1im][(FH)_{2.3}F]$, and (c) after 20 cycles in the $[C_2C_1pyrr][(FH)_{2.3}F]$ at 298 K.

Figure captions

Fig. 1 (a) Cyclic voltammograms and (b) initial charge–discharge curves of the copper metal electrode in the $[C_2C_1im][(FH)_{2.3}F]$ electrolyte at 298 K. Scan rate in (a): 10 mV s^{-1}. Charge–discharge rate in (b): 0.05C.

Fig. 2 X-ray diffraction patterns of the copper metal electrodes (a) before charging (pristine state), (b) after charging to 0.7 V vs. CuF_2/Cu, and (c) after 1 cycle to −0.3 V vs. CuF_2/Cu in the $[C_2C_1im][(FH)_{2.3}F]$ electrolyte at 298 K. The diffraction peaks of Pt metal arise from the Pt current collector.

Fig. 3 Cu 2*p* XPS profiles of the copper metal electrodes (a) before charging (pristine state), (b) after charging to 0.7 V vs. CuF_2/Cu, and (c) after 1 cycle to −0.3 V vs. CuF_2/Cu. in the $[C_2C_1im][(FH)_{2.3}F]$ electrolyte at 298 K.

Fig. 4 (a) Charge–discharge curves and (b) cycling characteristics of the copper metal electrode in the $[C_2C_1im][(FH)_{2.3}F]$ electrolyte at 298 K. Charge–discharge rate: 0.05C.

Fig. 5 (a) Charge–discharge curves of the copper metal electrode in $[C_2C_1pyrr][(FH)_{2.3}F]$ electrolyte at 298 K. (b) A comparison of discharge capacities of the copper metal electrode in the $[C_2C_1im][(FH)_{2.3}F]$ and $[C_2C_1pyrr][(FH)_{2.3}F]$ electrolytes at 298 K. Charge–discharge rate: 0.05C.

Fig. 6 SEM images and corresponding EDX mapping of the copper metal electrodes surfaces (a) before charging (pristine state), (b) after 20 cycles in the $[C_2C_1im][(FH)_{2.3}F]$, and (c) after 20 cycles in the $[C_2C_1pyrr][(FH)_{2.3}F]$ at 298 K.